Enhanced Carrier Mobility and Diffusion Length in Formamidinium-Rich Hybrid Perovskites: Effects of Grain-Size and Electron-Phonon Coupling

Mitko Oldfield,[†,‡,#] Gary Beane,[†,‡,#] Sebastian Fürer,[¶,@] Tan-Phat Nguyen,[†,#] Philippe Holzhey,[§] Boer Tan,[‖,@] Wenxin Mao,[⊥,@] Henry Snaith,[§] Udo Bach,[¶,@] and Agustin Schiffrin[*,†,#]

†*School of Physics and Astronomy, Monash University, Clayton, 3800, VIC, Australia*

‡*Contributed equally to this work*

¶*School of Engineering, Monash University, Clayton, 3800, VIC, Australia*

§*Clarendon Laboratory, Department of Physics, University of Oxford, Oxford, OX1 3PJ, United Kingdom*

‖*Oxford PV, Kidlington, OX5 1QU, United Kingdom*

⊥*Department of Chemical Engineering and Biotechnology, University of Cambridge, Cambridge, CB3 OAS, United Kingdom*

#*ARC Centre of Excellence in Future Low-Energy Electronics Technologies, Monash University, Clayton, 3800, VIC, Australia*

@*ARC Centre of Excellence in Exciton Science, Monash University, Clayton, 3800, VIC, Australia*

E-mail: agustin.schiffrin@monash.edu

Abstract

Carrier mobility, recombination rates and diffusion length directly govern the efficiency of hybrid lead-halide perovskites. Yet, their behavior across different carrier concentrations and the effects of microstructure remain poorly understood. Using time-resolved photoluminescence and optical pump - THz probe spectroscopy, we quantify mobility, carrier recombination rates and diffusion length for polycrystalline films of methylammonium (MA)- and formamidinium (FA)-rich lead-halide perovskites, across carrier concentrations ranging from $\sim 10^{15}$ to $\sim 10^{19}$ cm^{-3}. For example, at a carrier concentration of $\sim 10^{18}$ cm^{-3}, $FA_{0.95}MA_{0.05}Pb(I_{0.95}Br_{0.05})_3$ exhibits a mobility of 127 ± 9 cm^{2}V^{-1}s^{-1} and a diffusion length of 392 ± 85 nm, compared to 69 ± 1 cm^{2}V^{-1}s^{-1} and 139 ± 1 nm for $MAPbI_3$. These differences in mobility and diffusion length persist across different fluences, and are captured by a fluence-dependent rate model that accounts for both carrier generation and recombination at different material depths. From scanning electron microscopy and THz time-domain spectroscopy measurements, we attribute the increased mobility and diffusion length for the FA-rich perovskite mainly to a larger average grain size, after considering possible Fröhlich-type interactions between carriers and THz-active phonon modes. Our work establishes a mechanistic link between material microstructure and ultrafast carrier dynamics, informing crucial design principles for perovskite-based photovoltaic and optoelectronic applications.

Hybrid organic-inorganic lead halide perovskites, of the formula $APbX_3$, where A is an organic cation and X is a halogen atom, are strong candidates for active materials in efficient, inexpensive and versatile solar cells (SCs) and light-emitting devices.[1] Indeed, recent advances[2] in photovoltaic research have led to perovskite-only SCs with power conversion efficiencies exceeding 26%. Importantly, all of these solar cells use iodine as their main halide component.[3–9] A constraint arises in this class of three-dimensional perovskites, due to the corner-sharing nature of the lead iodide octahedra (PbI_6) (Figure 1a) – the organic cation must have an effective radius smaller than 2.6 Å to fit within the interstitial sites without compromising the structural integrity of the lattice. This leads to restrictions on the moieties

that may occupy the A site that allow the lead-halide perovskite to remain in its optically active phase.[4,10,11]

A common choice of cation that satisfies these conditions is methylammonium ($CH_3NH_3^+$, or MA). Indeed, MA-containing perovskites such as $MAPbI_3$ (MAPI) have been of great interest owing to their simple fabrication techniques and good charge-carrier transport characteristics.[12–14] However, over the past few years, perovskites with formamidinium ($CH(NH_2)_2^+$, or FA) as the cation have been shown to be superior for SCs because of their longer carrier lifetimes, greater fill factors (FF), increased short-circuit current densities (J_{SC}) and higher power conversion efficiencies (PCE) in comparison to MA-rich perovskites; see Figure 1c, d and Supporting Information (SI) Figure S1.[12–38]

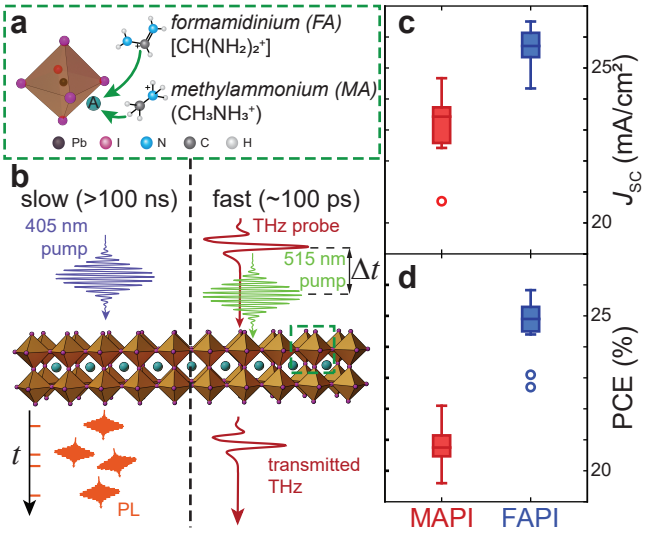

Figure 1: (a) Unit cell of lead-iodide perovskite showing inorganic octahedron and organic cation A (formamidinium, FA, or methylammonium, MA). (b) Schematic of techniques used to determine slow (>100 ns timescale) and fast (∼100 ps) carrier recombination mechanisms in lead-iodide perovskite film: time-resolved photoluminescence (trPL) and optical pump - THz probe (OPTP) spectroscopies. Green dashed box: perovskite unit cell as in (a). (c, d) Box-and-whisker plots of (c) short-circuit current density (J_{SC}) and (d) power conversion efficiency (PCE) for MA- and FA-rich lead-iodide perovskites, compiled from prior literature,[12–38] highlighting the better performance of FA-rich materials. Box limits: upper and lower quartile (25% and 75%). Horizontal line inside box: median value. Whiskers: upper (lower) quartile plus (minus) 1.5× interquartile range. Circles denote outliers.

The short-circuit current density, J_{SC}, and the open-circuit voltage, V_{OC}, (and therefore

PCE and FF) are directly related to the diffusion length, L_{D}, of charge carriers in a SC. Diffusion length is itself directly linked to charge carrier mobility, μ, and charge carrier recombination pathways, and is strongly influenced by carrier interactions and carrier lifetime within the material.[39,40]

While FA-rich devices typically outperform their MA-rich counterparts, the precise mechanistic origin of this advantage – especially across a wide range of carrier densities and at ultrafast timescales – is not yet fully resolved. Previous studies have focused extensively on low excitation fluences (i.e., low carrier concentrations), and/or cation-halide combinations other than FA-I or MA-I,[41–45] leaving a gap in terms of understanding how microstructure and carrier-phonon coupling might affect both μ and L_{D} in MAPI and FAPI in a broad range of operating conditions.

For instance, at low carrier density ($n \lesssim 10^{15}$ cm^{-3}), i.e., low photo-excitation fluences, the lifetime of carriers is predominantly dictated by their interaction with shallow electronic trap states of defects in the material;[46] such carrier recombination is non-radiative and monomolecular. At higher excitation fluences and carrier densities, all defect trap states become filled and free electrons and holes radiatively annihilate, with the evolution of the system at short timescales being dominated by bimolecular recombination.[39,47] When fluence and carrier density increase further, many-body Auger recombination begins to dominate, with electrons and holes recombining non-radiatively by transferring energy to other electrons or holes which then decay to the band edge via phonon-assisted cooling.[48,49] At significant carrier concentrations ($n \gtrsim 10^{15}$ cm^{-3}), non-radiative Auger and radiative bimolecular recombination in lead-halide perovskites can unfold at timescales of ∼tens and ∼hundreds of ps, respectively, significantly reducing carrier lifetime and hence affecting perovskite SC efficiency.[50]

Recent works have highlighted the impact that Auger carrier recombination has on J_{SC}, V_{OC}, L_{D} and μ, with maximum efficiency under typical operation conditions (i.e., $n \approx 10^{15}$ cm^{-3}) requiring Auger recombination rate constants smaller than $\sim 10^{-31}$ cm^{6}s^{-1}; there

is a significant reduction in V_{OC} and PCE for higher Auger recombination rates.[50] The interplay between non-radiative Auger recombination and radiative bimolecular electron-hole recombination is also important for light-emitting applications involving perovskites, such as perovskite-based lasers[51,52] and light-emitting diodes.[1]

Previous studies have investigated mobility, μ, and diffusion length, L_D, in lead-halide perovskites utilising techniques such as time-resolved microwave conductivity and time-resolved photoluminescence (trPL).[53–57] However, these techniques suffer from limited temporal resolution – typically on the order of nanoseconds (ns) – and are incapable of capturing the real-time relaxation of carriers due to bimolecular and Auger recombination at relevant carrier densities, where these high-order processes can unfold at sub-ns timescales. Thus, such methods are typically restricted to low carrier concentrations ($n \lesssim 10^{15}$ cm^{-3}) – i.e., low incident light intensities – where monomolecular defect-induced trap recombination (with a time constant on the order of ns that is independent of carrier density) is dominant. At higher incident light intensities and carrier concentrations, omitting higher-order recombination processes (e.g. bimolecular, Auger) leads to significant errors in the determination of μ and L_D.[58,59]

Optical pump - THz probe (OPTP) spectroscopy can track carrier populations in real time with picosecond (ps) and even sub-ps resolution, capturing higher order recombination mechanisms. Previous studies have investigated carrier mobility in lead-halide perovskites using OPTP spectroscopy,[44,45,60] in particular, comparing the roles of the organic cations FA and MA in lead bromide (Br) perovskites ($APbBr_3$, where A = FA or MA).[56] However, OPTP has not been used so far to compare the roles of FA and MA in lead-iodide perovskites ($APbI_3$), which are of substantially greater interest for SC applications due to their increased absorption at longer visible wavelengths due to a reduced bandgap energy.[61,62]

In this study, we utilize trPL and OPTP spectroscopy (Figure 1b) to track charge carrier recombination processes in ∼500-nm-thick MA-rich ($MAPbI_3$, herein referred to as MAPI) and FA-rich [$FA_{0.95}MA_{0.05}Pb(I_{0.95}Br_{0.05})_3$, herein referred to as FAPI] perovskite films (see

SI for sample preparation), in real time, with ps resolution and µs range. These films were prepared using identical synthesis techniques to films produced for optimized devices, making them representative of SC-ready thin films.[10,11,53] These time-resolved measurements allow us to retrieve the charge carrier mobility, μ, total effective carrier recombination rate, Γ_{tot}, and carrier diffusion length, L_{D}, for both types of materials, within a broad range of incident visible light fluences and carrier densities. We infer that $\mu_{\mathrm{FAPI}} > \mu_{\mathrm{MAPI}}$, $\Gamma_{\mathrm{tot}}^{(\mathrm{FAPI})} < \Gamma_{\mathrm{tot}}^{(\mathrm{MAPI})}$, and $L_{\mathrm{D}}^{(\mathrm{FAPI})} > L_{\mathrm{D}}^{(\mathrm{MAPI})}$ for the range of excitation fluences and carrier densities considered, confirming preferential properties of FAPI for SC applications. We mainly attribute these differences to a significantly larger average grain size – with average characteristic length $\langle l_{\mathrm{grain}} \rangle$ characterized via scanning electron microscopy (SEM) – for FAPI in comparison with MAPI. We infer no noticeable differences between the two materials in terms of possible long-range (i.e. Fröhlich-type) interactions between carriers and THz-active phonons – detected via THz time-domain spectroscopy (THz-TDS). These findings emphasize the need to optimize material grain size in order to extend diffusion lengths, critical for SC and high-fluence optoelectronic applications (e.g. LEDs, lasers).

The trPL and OPTP data in Figure 2 reveal the time evolution of the charge carrier population for MAPI and FAPI at slow (10 ns resolution, ∼1 µs range) and fast (1.5 ps resolution, ∼1 ns range) timescales, respectively (see SI for details on experimental methods). For both types of measurements, the pump photon energy (2.93 eV for trPL, 2.41 eV for OPTP) lies well within the absorption band of both MAPI and FAPI (see SI Figure S3), with absorption coefficients at 2.41 eV estimated as $\alpha_{\mathrm{abs}}^{(\mathrm{FAPI})} = (3.5 \pm 0.5) \times 10^4$ cm^{-1} and $\alpha_{\mathrm{abs}}^{(\mathrm{MAPI})} = (2.7 \pm 0.2) \times 10^4$ cm^{-1}, and penetration depths $1/\alpha_{\mathrm{abs}}^{(\mathrm{FAPI})} = 285 \pm 44$ nm and $1/\alpha_{\mathrm{abs}}^{(\mathrm{MAPI})} = 371 \pm 28$ nm, smaller than the film thicknesses of 494 ± 15 nm and 589 ± 20 nm. This means that the trPL and OPTP data are related to the intrinsic material properties, and are not dependent on material thickness. Absorbance measurements (see SI) indicate exciton binding energies $E_{\mathrm{B}}^{(\mathrm{MAPI})} = 30 \pm 12$ meV and $E_{\mathrm{B}}^{(\mathrm{FAPI})} = 20 \pm 11$ meV, within the broad range previously reported in the literature.[48,63–70] These exciton binding energies are

relatively low, similar to the thermal energy $k_{\mathrm{B}}T \approx 26$ meV at room temperature (RT). We therefore assume that at RT excitons quickly dissociate to free carriers and excitonic effects are relatively insignificant in our experiments.[48,71,72] The trPL curves in Figure 2a are obtained at low photo-excitation fluence and hence low photo-induced carrier densities, where monomolecular recombination is faster than and dominates over higher order bimolecular and Auger recombination[44,48,71,73,74] (see SI). These curves are therefore well-fit by a single decaying exponential function, yielding carrier relaxation time constants $\tau_1^{(\mathrm{MAPI})} = 307$ ns and $\tau_1^{(\mathrm{FAPI})} = 445$ ns, in good agreement with previous literature.[44,75,76] The trPL signal is proportional to the radiative bimolecular electron-hole recombination rate – which, at the low fluence considered, is slow (i.e., inefficient) – and to the carrier density at a given time t, which, at such a low fluence, is dominated by faster monomolecular non-radiative electron trapping via defect states. That is, the trPL decay rates $\Gamma_1^{(\mathrm{MAPI})} = k_1^{(\mathrm{MAPI})} = 1/\tau_1^{(\mathrm{MAPI})}$ and $\Gamma_1^{(\mathrm{FAPI})} = k_1^{(\mathrm{FAPI})} = 1/\tau_1^{(\mathrm{FAPI})}$ are associated with monomolecular trap-assisted carrier recombination[39,51,72] The slower monomolecular recombination in FAPI suggests a reduced number of available trap states – indicating fewer defects within the material.[49] Previous work investigating mixed FA/MA perovskites also finds a longer monomolecular lifetime for FA-rich systems.[77]

The OPTP measurements in Figure 2b, c show the relative change in THz transmission, $-\Delta T/T$, for both MAPI and FAPI, as a function of pump-probe time delay, Δt. We considered optical pump fluences $\sim 90 < F < \sim 570$ μJ cm^{-2} (see SI for details on experimental methods). The ∼1.5 ps resolution of these OPTP measurements allow for tracking the time evolution of carrier recombination processes unfolding at timescales not accessible by trPL spectroscopy. The negative change in THz transmission for $\Delta t > 0$ is the result of increased THz absorption by charge carriers excited by the visible pump pulse. The subsequent change in $\Delta T/T$ indicates at least one fast carrier relaxation channel (e.g. with a time constant $< \sim 10$ ps) and at least one slower decay channel (time constant between ∼100 ps and ∼1 ns). The magnitude $|\Delta T/T|$ correlates with the density of photo-excited carriers, increasing

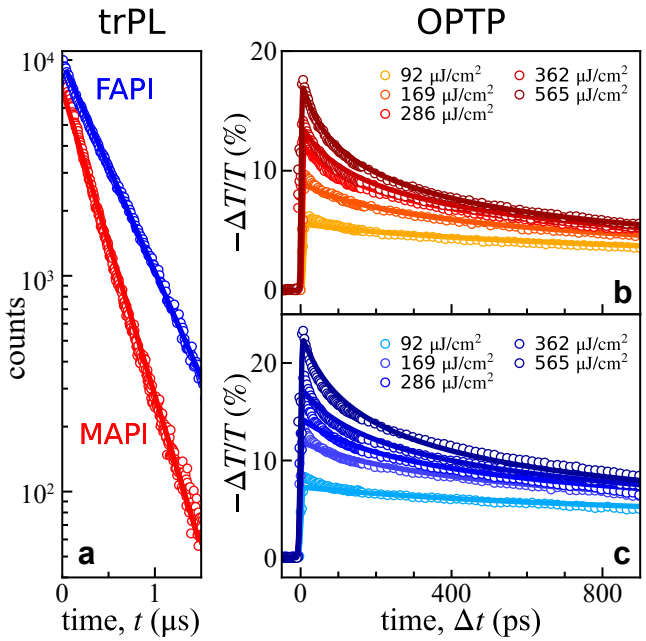

Figure 2: (a) Time-resolved photoluminescence (trPL) signal as a function of time for MAPI (red) and FAPI (blue) films. Circles: experimental data. Solid curves: single-exponential fits. (b, c) Change in THz transmission as a function of time delay, Δt, between optical pump pulse (with central wavelength $\lambda_{\text{pump}} = 515$ nm) and THz probe waveform, for an individual sample of MAPI (red) and FAPI (blue), for different incident pump fluences. Markers: experimental data. Solid curves: fits according to Eq. 1, with k_2 and k_3 as fitting parameters, and k_1 fixed according to trPL measurements in (a). These curves enable retrieval of effective carrier mobilities and diffusion lengths.

with fluence F.

Using the monomolecular recombination time constant τ_1 (i.e. with rate constant $k_1 = \Gamma_1 = 1/\tau_1$, determined by the single exponential fit of the trPL data), and the knowledge of additional fast (time constant $< \sim$100 ps) and slow (time constant between $\sim$100 ps and $\sim$1 ns) recombination channels identified from the OPTP data (Figure 2b, c), we fit the time- and fluence-dependent change in transmission $(-\Delta T/T)(\Delta t, F)$ in Figure 2b, c by assuming that it is proportional to the total carrier density within the material at a time Δt after photo-excitation:

$$-\frac{\Delta T}{T}(\Delta t, F) = \xi \int_0^d n(\Delta t, F, z) dz \tag{1}$$

where ξ is a proportionality factor and $n(\Delta t, F, z)$ is the carrier density at a depth z within the perovskite film with thickness d. We used a rate model[44,45,75,76,78] to account for the time evolution of $n(\Delta t, F, z)$, taking into account both generation and recombination of photo-excited carriers:

$$\frac{\partial n(\Delta t, F, z)}{\partial t} = \zeta(\Delta t, z) - k_3 \cdot n(\Delta t, F, z)^3 - k_2 \cdot n(\Delta t, F, z)^2 - k_1 \cdot n(\Delta t, F, z) \qquad (2)$$

Here, k_2 and k_3 are second-order and third-order recombination rate constants, respectively, and $\zeta(t, z)$ accounts for the z-dependent photo-generation of carriers:

$$\zeta(\Delta t, z) = \beta(F) \cdot F \cdot \exp\left[-\frac{(\Delta t - t_0)^2}{\tau_{\text{eff,res}}^2}\right] \cdot \exp(-\alpha_{\text{abs}} z) \qquad (3)$$

where $\beta(F)$ is a proportionality factor, t_0 is a time offset, $\tau_{\text{eff,res}}$ is the system's effective response (given by the convolution between optical pump and THz probe pulses), and α_{abs} is the material's absorption coefficient at the excitation wavelength $\lambda_{\text{pump}} = 515$ nm (as defined above). We used ξ, k_2, k_3 and $\tau_{\text{eff,res}} \approx 3$ ps as global fitting parameters (i.e., fluence independent), and β (accounting for potential saturation effects; see SI) and t_0 as local fitting parameters (i.e. fluence dependent). We fixed k_1 to the values determined from trPL. Note that this rate model explicitly takes into account generation of photo-excited carriers explicitly, in contrast with rate models used previously for carrier recombination in metal-halide perovskites.[44]

Equations 1 - 3 yield an excellent fit of the OPTP data, for the full Δt range of $\sim$1 ns, and for all optical pump fluences considered (Figure 2b, c). This fit results in fluence-independent recombination rate constants $k_2^{(\text{MAPI})} = (14.8 \pm 9.9)\ \times 10^{-11}$ cm^3 s^{-1}, $k_2^{(\text{FAPI})} = (1.2 \pm 0.9) \times 10^{-11}$ cm^3 s^{-1}, $k_3^{(\text{MAPI})} = (7.7 \pm 0.9)\ \times 10^{-27}$ cm^6 s^{-1} and $k_3^{(\text{FAPI})} = (1.8 \pm 0.6)$ $\times 10^{-27}$ cm^6 s^{-1} (uncertainty relates to the standard error across different films of the same material). While these rate constant values for MAPI are consistent with previous litera-

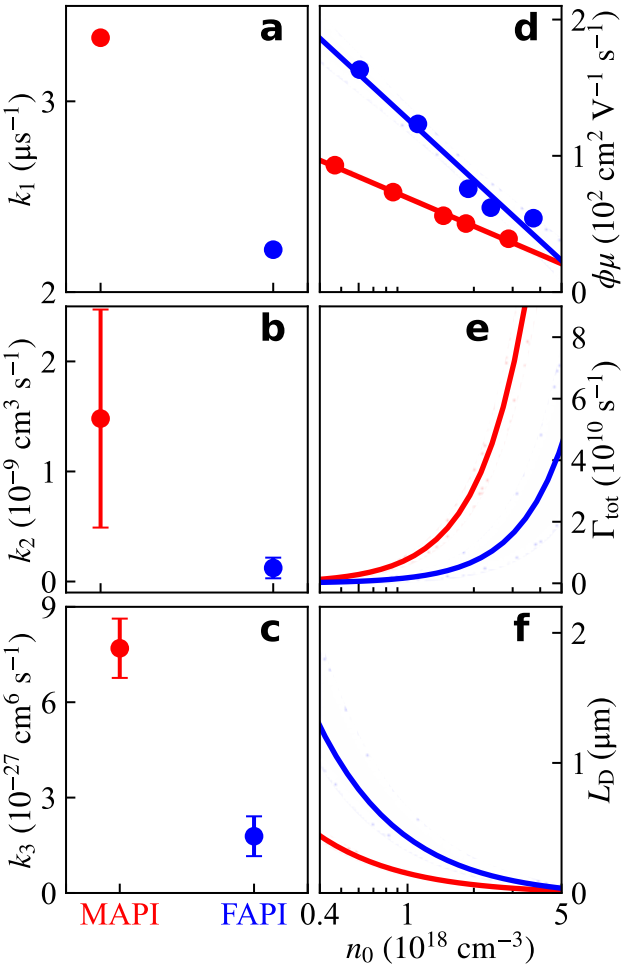

Figure 3: (a - c) Carrier recombination rate constants for MAPI (red) and FAPI (blue), determined by fitting trPL (one film of each material; single-exponential fit) and OPTP data (four films of each material; based on Eqs. (1) - (3); error bars: standard error). We ascribe k_1, k_2 and k_3 to monomolecular, bimolecular and Auger-type recombination processes, respectively. (d - f) Effective carrier mobility, $\phi\mu$ (see SI for calculation), total carrier recombination rate, Γ_{tot} (calculated via Eq. (4), with $k_1 ... k_3$ from (a - c)), and carrier diffusion length, L_D (calculated via Eq. (5)), as a function of initial photo-excited carrier density $n_0 = n(\Delta t = 0)$, for MAPI (red) and FAPI (blue). Solid curves in (d): $(\phi\mu)(n) \propto \ln(n_0)$ fit. Filled circles: averages across different films considered. Shaded areas: standard error.

ture,[44] to our knowledge these are the first reported carrier recombination rate constants for FAPI.

From these results, we infer that the second-order term in Eq. (2) can be associated with bimolecular carrier recombination, and the third-order term with faster Auger-type

recombination, based on the characteristic recombination rate constants k_2 and k_3 obtained by the fitting procedure, comparable to values reported previously.[44,67,73,75,76,78] That is, for the excitation fluences considered, Auger recombination is substantial and dominates other recombination processes at small Δt (i.e. where the carrier density n is significantly large). Sequentially, as Δt increases and n decays, bimolecular recombination and then monomolecular recombination dominate in turn.[51,52,79,80] Notably, $k_2^{(\mathrm{MAPI})} > k_2^{(\mathrm{FAPI})}$ (Figure 3b), and $k_3^{(\mathrm{MAPI})} > k_3^{(\mathrm{FAPI})}$ (Figure 3b); both bimolecular and Auger-type recombination rates are larger for MAPI than for FAPI.

Previous works have also utilized rate models to describe the time evolution of hot carrier density in lead-halide perovskites and its relaxation via monomolecular, bimolecular and Auger recombination.[44,45,75,76,78] Our model is fully consistent with these previous approaches, and takes into account both the excitation fluence dependence of the recombination and the depth-dependence of the carrier concentration induced by the pump pulse. Moreover, our model considers not only the relaxation of photo-excited carriers, but also their initial fluence- and time-dependent generation by the pump. This allows us to consider potential carrier saturation effects – accounted for by $\beta(F)$ in Eq. (3) – that likely occur at the higher fluences F (and hence initial carrier densities n_0 upon photo-excitation) of our experiments – $F \approx 90$ to 600 μJ/cm^2 and $n_0 \approx 10^{17}$ to 10^{18} cm^{-3} (i.e. including values above $\sim 10^{18}$ cm^{-3} where Auger recombination begins to dominate) – compared to these previous studies where $F \lesssim 50$ μJ/cm^2.

We can derive an effective carrier mobility, $\mu_{\mathrm{eff}} = \phi\mu \propto |(\Delta T/T)\,(\Delta t = 0)|$, via the maximum relative change in THz transmission, $|\Delta T/T|$ at $\Delta t = 0$, in our OPTP measurements (Figure 2b, c),[44] for both MAPI and FAPI, as a function of initial carrier density n_0 (Figure 3d; see SI for details, including calculation of n_0 from fluence F). Here, we assume a photon-to-charge branching ratio of $\phi = 1$ (i.e., one incident photon generates one carrier), as in previous works;[44] our OPTP data at $\Delta t = 0$ therefore provides a lower-bound estimate of μ. The carrier mobility of FAPI and MAPI decreases as a function of n_0, varying from $\sim$180 to

$\sim$50 cm^{2}V^{-1}s^{-1} and from $\sim$100 to $\sim$40 cm^{2}V^{-1}s^{-1}, respectively, as n_0 varies from $\sim 5 \times 10^{17}$ to $\sim 5 \times 10^{18}$ cm^{-3}, with $\mu_{\text{eff}}^{(\text{FAPI})}$ substantially higher than $\mu_{\text{eff}}^{(\text{MAPI})}$ for all considered n_0 (Figure 3d). We fit $\mu_{\text{eff}}(n_0)$ empirically as $\phi\mu \propto \ln(n_0)$, which agrees well with previous literature[58] at carrier concentrations above 10^{14} cm^{-3}; this allows us to estimate values of μ_{eff} for n_0 outside the considered fluence range. For instance, $\mu_{\text{eff}}^{(\text{FAPI})}/\mu_{\text{eff}}^{(\text{MAPI})} \approx 1.9$ at $n_0 \approx 4 \times 10^{17}$ cm^{-3}, and $\mu_{\text{eff}}^{(\text{FAPI})}/\mu_{\text{eff}}^{(\text{MAPI})} \approx 1.1$ at $n_0 \approx 5 \times 10^{18}$ cm^{-3}. That is, within the range of charge carrier densities investigated, we see a carrier mobility in FAPI that is higher than MAPI. Note that at typical device carrier densities ($n_0 \approx 10^{15}$ cm^{-3}) we estimate $\mu_{\text{eff}}^{(\text{FAPI})}/\mu_{\text{eff}}^{(\text{MAPI})} \approx$ 2.1.

From $k_1 ... k_3$ resulting from the fits of trPL and OPTP data (Figure 3a-c), we can define an effective total carrier recombination rate as a function of initial carrier density n_0:

$$\Gamma_{\text{tot}}(n_0) = \Gamma_3(n_0) + \Gamma_2(n_0) + \Gamma_1 = k_3 \cdot n_0^2 + k_2 \cdot n_0 + k_1 \tag{4}$$

Here, $\Gamma_j = k_j \cdot n_0^{j-1}$ ($j = 1...3$) are the carrier relaxation rates at different carrier densities, with slow monomolecular recombination (associated with Γ_1) dominating at low n_0, and faster bimolecular and Auger-type recombination processes (associated with Γ_2 and Γ_3) dominating the initial instances of relaxation at high n_0. As n_0 increases, bimolecular and Auger-type recombination processes become more likely, resulting in a larger Γ_{tot} (Figure 3e).

From μ_{eff} and Γ_{tot}, we may estimate the charge carrier diffusion length in our materials, L_D, as a function of n_0 (Figure 3f), using[44]

$$L_{\text{D}}(n_0) = \sqrt{\frac{\phi\mu(n_0) k_{\text{B}} T}{|e| \Gamma_{\text{tot}}(n_0)}} \tag{5}$$

where k_{B} is Boltzmann's constant, T is temperature (300 K), and e is the electron charge. The decrease of μ_{eff} and increase of Γ_{tot} with n_0 results in a nonlinear, exponential-like decay of L_{D} as a function of n_0, with $L_{\text{D}}^{(\text{FAPI})}$ larger than $L_{\text{D}}^{(\text{MAPI})}$ for all considered n_0. Note that

$L_{\mathrm{D}}^{(\mathrm{FAPI})} \approx L_{\mathrm{D}}^{(\mathrm{MAPI})}$ as $n_0 \gtrsim 5 \times 10^{18}$ cm^{-3}, mainly due to the fact that $\mu_{\mathrm{eff}}^{(\mathrm{FAPI})} \approx \mu_{\mathrm{eff}}^{(\mathrm{MAPI})}$ as $n_0 \gtrsim 5 \times 10^{18}$ cm^{-3} (Figure 3d). We may use the fits of $\mu_{\mathrm{eff}}(n_0)$ in Figure 3d, and $k_1 ... k_3$ in Figure 3a-c (which determine $\Gamma_{\mathrm{tot}}(n_0)$ in Figure 3e), to estimate L_{D} at a carrier density $n_0 \approx 10^{15}$ cm^{-3} typically seen in an operating lead-halide perovskite SC.[81] We find $L_{\mathrm{D}}^{(\mathrm{MAPI})} \approx 14.3$ μm and $L_{\mathrm{D}}^{(\mathrm{FAPI})} \approx 25.7$ μm. This increased diffusion length in FAPI is consistent with previous reports.[81] The decay in L_{D} with increasing n_0, for both MAPI and FAPI, from several microns to hundreds of nanometers, also agrees well with previous observations.[82]

In the following, we attempt to rationalize the differences in carrier mobility, total recombination rate and diffusion length for MAPI and FAPI, by considering their microscopic morphology and THz-active phonon modes. The distribution of characteristic visible grain lengths for MAPI and FAPI (Figure 4a) determined via SEM (Figure 4b, c) shows a median grain length for FAPI which is approximately double that of MAPI. For MAPI, the grains are smaller, but with a more uniform size distribution. In FAPI, substantially larger grains are intercalated with smaller grains. Grain boundaries can act as centers for electron-hole recombination.[83] We therefore hypothesize that the larger effective carrier mobility μ_{eff} and smaller total recombination rate Γ_{tot} (and hence significantly larger diffusion length L_{D}; Figure 3c-d) in FAPI are due – at least partially – to the larger grains (540 ± 300 nm vs. 200 ± 90 nm) and to a reduced number of grain boundaries. Note that the smaller monomolecular recombination rate in FAPI, $k_1^{(\mathrm{FAPI})} = \Gamma_1^{(\mathrm{FAPI})}$ (Figures 2a, 3a), suggests a reduced number of available trap states, indicative of fewer defects,[49] and consistent with the larger mean visible grain size and smaller total grain boundary surface area. Larger grains have consistently been associated with larger carrier mobilities in perovskites and other semiconductors.[84,85] The increased FAPI diffusion length can also be linked to a substantially faster reorientation[86,87] of the organic cation FA^+, which can potentially stabilize carriers and promote longer hot-carrier lifetimes.[81] Note that the larger μ_{eff} and L_{D} for FAPI is also consistent with reduced electronic dynamic disorder in FA-based systems – due to sparsely distributed

isotropic nanodomains as opposed to dense anisotropic nanodomains – in comparison with MA-based systems.[88]

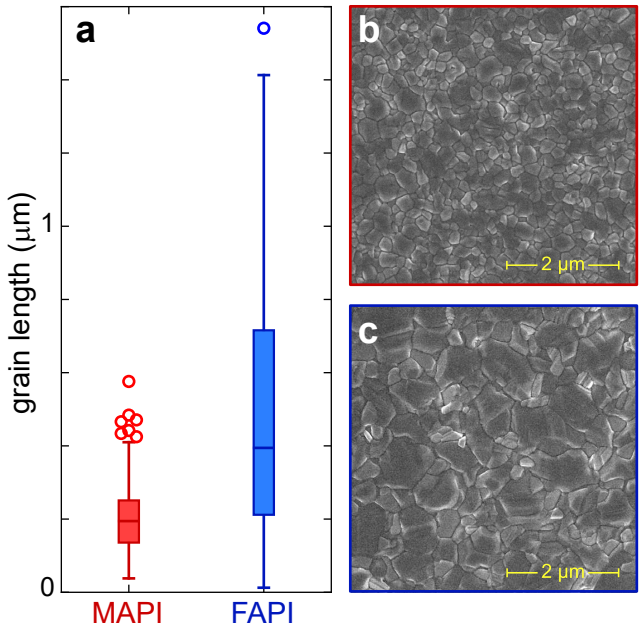

Figure 4: (a) Characteristic grain lengths for two MAPI (red) and two FAPI (blue) films, determined by randomly selecting 50 grains within a 20 µm × 20 µm sample area and measuring the average of their major and minor axes. Box limits are upper and lower quartile (25% and 75%); horizontal line inside box denotes median value. Whiskers are upper (lower) quartile plus (minus) 1.5× interquartile range. Outliers are denoted by circles. Mean grain length for MAPI (FAPI): 200 ± 90 nm (540 ± 300 nm). (b, c) Examples of SEM images of MAPI (b) and FAPI (c) sample areas.

We further performed THz-TDS (i.e., without photo-excitation of the material), allowing us to retrieve the complex dynamic electrical conductivity $\tilde{\sigma}(\omega)$ of the MAPI and FAPI films within the $0.35-5$ THz spectral range (see SI for details). Both the real (σ_1) and imaginary (σ_2) parts of $\tilde{\sigma}(\omega)$ for MAPI and FAPI are qualitatively similar, with $\sigma_1(\omega)$ showing two prominent peaks at frequencies corresponding to inflection points of $\sigma_2(\omega)$ (Figure 5). We fit $\sigma_1(\omega)$ and $\sigma_2(\omega)$ simultaneously using a Lorentz two-oscillator model:[89]

$$\tilde{\sigma}(\omega) = -i\varepsilon_0\omega(\varepsilon_\infty - 1) + \sum_{m=1,2} \frac{\varepsilon_0\omega_{\mathrm{p},m}^2\omega}{i(\omega_{0,m}^2 - \omega^2) + \omega\Gamma_m} \tag{6}$$

where $\omega_{\mathrm{p},m}$, $\omega_{0,m}$ and Γ_m are the plasma frequency, oscillator resonance frequency and os-

cillator scattering rate of the m^{th} oscillator, respectively ($m = 1, 2$). Here, ε_∞ is the high-frequency dielectric constant.

This fit yields $\omega_{0,1}^{(\text{MAPI})}/(2\pi) = 0.85 \pm 0.01$ THz, $\omega_{0,2}^{(\text{MAPI})}/(2\pi) = 1.85 \pm 0.01$ THz, $\omega_{0,1}^{(\text{FAPI})}/(2\pi) = 0.79 \pm 0.01$ THz, and $\omega_{0,2}^{(\text{FAPI})}/(2\pi) = 1.72 \pm 0.01$ THz. We attribute these two oscillators to THz-active lattice vibrational modes (i.e. transverse optical phonons), namely twisting and stretching of the inorganic octahedra at low frequency, and nodding-donkey (i.e., rotational vibration modes around the organic cation C or N atoms) and lurching (related to both cation and inorganic octahedra motion) modes at higher frequency.[90,91] The inorganic octahedra twisting and stretching mode peak at ∼0.9 THz is very similar for both perovskites, owing to their quasi-identical inorganic composition. Conversely, the nodding-donkey and lurching mode peak is substantially different, in both amplitude and frequency position (see SI for obtained best fit parameters). The lower frequency of the cation-related mode in FAPI can be explained by the greater molecular weight of FA^+ in comparison to MA^+.

Terahertz TDS is sensitive to transverse optical (TO) phonon modes, as opposed to longitudinal (LO). However, the motion of the inorganic octahedra – to which both Lorentzian peaks in σ_1 in Figure 5a are associated – leads to local symmetry-breaking, giving these modes both TO and LO character.[90] By considering the loss function $-\text{Im}[1/\tilde{\varepsilon}(\omega)]$, where $\tilde{\varepsilon}(\omega) = 1 + i\tilde{\sigma}(\omega)/(\omega\varepsilon_0)$ is the complex permittivity, and fitting this loss function with a sum of two Lorentzians with amplitudes A_1 and A_2 centered at angular frequencies $\omega_{\text{LO, 1}}$ and $\omega_{\text{LO, 2}}$ (see Figure S12 in SI), we may estimate the angular frequency of an effective LO-character phonon mode (associated with the TO-character phonon modes with angular frequencies $\omega_{0,1}$ and $\omega_{0,2}$ above):

$$\omega_{\text{LO, eff}}^2 = \frac{\sum_{m=1,2} A_m^2}{\sum_m (A_m^2/\omega_{\text{LO, m}}^2)} \tag{7}$$

We extract $\omega_{\text{LO, eff}}^{(\text{MAPI})}/2\pi = 2.81 \pm 0.02$ THz and $\omega_{\text{LO, eff}}^{(\text{FAPI})}/2\pi = 2.86 \pm 0.02$ THz. Polar semiconductors (such as perovskites) have an upper limit of carrier mobility dictated by

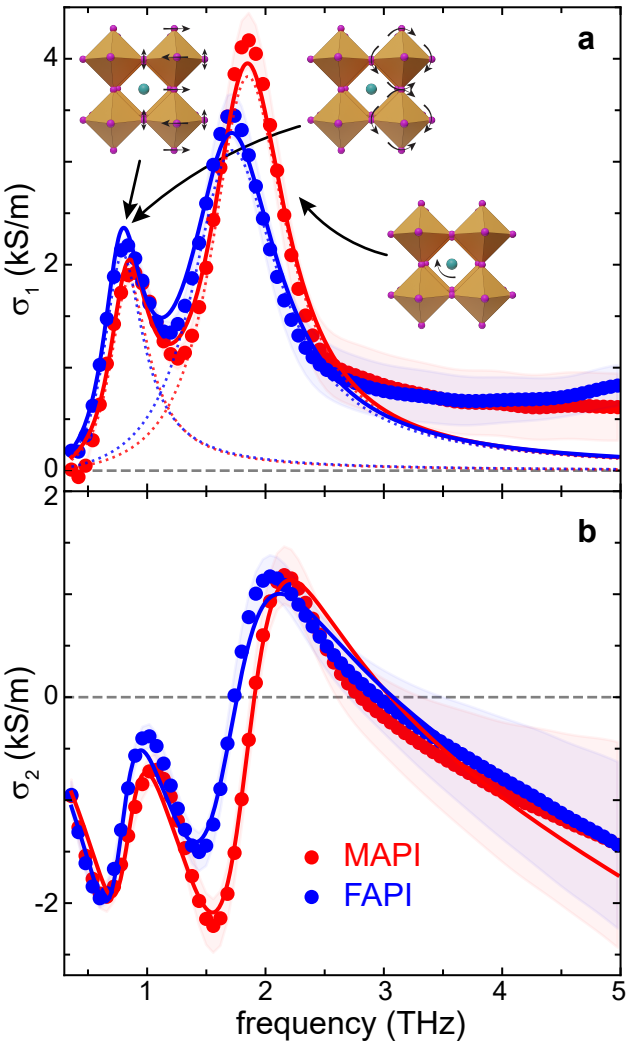

Figure 5: (a) Real and (b) imaginary parts of THz conductivity as a function of frequency for non-excited (i.e., without optical pump pulse) MAPI (red) and FAPI (blue). Filled circles: experimental data (average across three positions of five different samples of each perovskite). Solid curves: fits of $\sigma_1(\omega)$ and $\sigma_2(\omega)$ using Lorentz model Eq. (6). Dotted curves: Lorentzian fit peaks for $\sigma_1(\omega)$. Shaded area: standard error of experimental data. We attribute the low-frequency (high-frequency) Lorentzian peak in $\sigma_1(\omega)$ to twisting and stretching of the inorganic octahedra (nodding-donkey and lurching modes involving the organic cation), respectively.[90]

LO phonon scattering. This upper bound mobility can be estimated via Feynman's polaron theory,[92] and, for large (Fröhlich) polarons, is given by:[93]

$$\mu_{\mathrm{ph}} = \frac{3e}{m_{\mathrm{b}}^{*}} \frac{\sqrt{\pi}\sinh\left(\beta_{\mathrm{F}}/2\right)}{\omega_{\mathrm{LO,\,eff}}\,\alpha_{\mathrm{F}}\,\beta_{\mathrm{F}}^{5/2}} \left(\frac{w}{v}\right)^{3} \frac{1}{K(a,b)} \tag{8}$$

Here, m_{b}^{*} is the carrier effective band mass, $\alpha_{\mathrm{F}} = 1/4\pi\sqrt{m_b^* e^4(/2\hbar^3 \varepsilon_*^2 \omega_{\mathrm{LO,\,eff}}}$) is the carrier-phonon coupling constant (with $\varepsilon_* = [1/\varepsilon_\infty - 1/\varepsilon_S]^{-1}$ the ionic screening parameter and ε_S the static dielectric constant), and $\beta_{\mathrm{F}} = \hbar\omega_{\mathrm{LO,\,eff}}/(k_B T)$. Parameters w and v are determined from the minimization[92,93] of the Osaka free energy for an LO phonon at a given temperature T, and $K(a,b) = \int_0^\infty dx[x^2 + a^2 - b\cos(vx)]^{-3/2}\cos(x)$, where $a^2 = (\beta_{\mathrm{F}}/2)^2 + [(v^2 - w^2)/(w^2 v)]\beta_{\mathrm{F}}\coth(\beta v/2)$, and $b = [(v^2 - w^2)/(w^2 v)]\beta_{\mathrm{F}}\sinh(\beta_{\mathrm{F}} v/2)$ (see Table 4 in SI).

By assuming m_{b}^{*} equal to the effective electron mass (i.e. $m_{\mathrm{b}}^{*(\mathrm{MAPI})} = m_{\mathrm{e}}^{*(\mathrm{MAPI})} = 0.228\,m_0$ and $m_{\mathrm{b}}^{*(\mathrm{FAPI})} = m_{\mathrm{e}}^{*(\mathrm{FAPI})} = 0.218\,m_0$ based on theory[70,94]), ε_∞ as determined by the Lorentz oscillator model fit of $\tilde{\sigma}(\omega)$ above (Table 2 in SI), $\varepsilon_S \approx \mathrm{Re}[\tilde{\varepsilon}(\omega/(2\pi) \approx 0.35\,\mathrm{THz})]$ (i.e. experimental low-frequency limit; Figure S11c in SI), and $T = 298$ K (to match experiments), we obtain $\alpha_{\mathrm{F}}^{(\mathrm{MAPI})} = 1.35$ and $\alpha_{\mathrm{F}}^{(\mathrm{FAPI})} = 1.45$. This is well within the large (Fröhlich) polaron regime[94,95] (i.e. $\alpha_{\mathrm{F}} < 6$), justifying the use of Equation (8). Note that the values used for ε_S are consistent with the Cochran-Cowley relation[96] (see SI). And from Equation (8) we obtain $\mu_{\mathrm{ph}}^{(\mathrm{MAPI})} = 320$ cm^{2}V^{-1}s^{-1} and $\mu_{\mathrm{ph}}^{(\mathrm{FAPI})} = 324$ cm^{2}V^{-1}s^{-1}, similar to literature values derived using the same technique.[97,98]

The negligible difference in μ_{ph} between the two perovskites suggests that the impact of changing the organic cation (MA/FA) on carrier-phonon interactions is minimal. We would expect a difference in organic cation to have some impact on the nodding-donkey and lurching phonon modes, since these modes involve motion of the organic cation.[90] The σ_1 peak in Figure 5a with characteristic angular frequency $\omega_{0,2}$, associated with these modes, is substantially different for the two materials, with its amplitude being ~25 % larger for MAPI. Yet, the loss function $-\mathrm{Im}[1/\tilde{\varepsilon}(\omega)]$ is very similar for both materials (within the THz spectral range considered; see Figure S12 in SI), leading to very small deviations in the effective LO phonon mode angular frequency, $\omega_{\mathrm{LO,\,eff}}$, and hence in μ_{ph}.

From this we infer that the differences in mobility, carrier recombination rate and diffusion length between MAPI and FAPI (Figure 3d-f) result mostly from differences in crystal grain

size and film quality.

Further studies are required to reliably and quantitatively determine possible differences in carrier mobility between MAPI and FAPI due to carrier-phonon interactions. Note that thermalization and initial steps of relaxation of hot carriers occur on sub-ps timescales, and whilst this cooling can be prolonged by Auger heating of carriers and the hot-phonon bottleneck effect,[66,75,99,100] our OPTP time resolution (∼1.5 ps) may not capture the full response around $\Delta t = 0$. This means that our measured values of $|\,(\Delta T/T)\,(\Delta t = 0)|$ may be smaller than those obtainable with higher time-resolution; our estimates of μ_{eff} for MAPI and FAPI should be regarded as lower bounds.

In conclusion, our work highlights substantially higher carrier mobility, smaller carrier recombination rate and greater carrier diffusion length in FA-rich lead halide perovskites, when compared to their MA-rich counterparts. By utilizing time- and frequency-resolved spectroscopy techniques (spanning timescales from 1 ps to 1 μs, and a broadband spectral range from ∼0.35 to 5 THz, respectively), supported by microstructure information (provided by SEM), we show that these differences can be mainly associated with fewer grain boundaries (acting as carrier scattering sites) in FAPI, with no evidence of significant differences between the two materials in terms of interactions between carrier and THz-active phonons. It is important to emphasize that our study complements previous works,[19,42,43,45,101] by providing a direct comparison between MAPI and FAPI in terms of carrier properties. This study prompts further investigation into carrier relaxation kinetics and dynamics in lead-halide perovskites, in particular regarding carrier properties at grain boundaries and carrier-phonon interactions, at sub-picosecond timescales and varying carrier densities. This could lead to further fundamental findings on carrier mobility, carrier recombination rate and diffusion length, crucial for the development of light-harvesting and optoelectronic technologies based on these materials. The approach outlined in this work provides a blueprint for correlating ultrafast carrier dynamics with microstructure, allowing for the rational design of perovskite films for high-fluence applications (e.g. photovoltaics,

lasers).

Associated Content

Data Availability Statement The data supporting the findings of this study are available from the authors upon reasonable request.

Supporting Information The Supporting Information (SI) is available free of charge at XXX, including details of: Open circuit voltage and fill factor for MAPI and FAPI; Perovskite synthesis [$MAPbI_3$, $FA_{0.95}MA_{0.05}Pb(I_{0.95}Br_{0.05})_3$]; Spectroscopy techniques (X-ray diffraction, VIS-IR Spectrophotometry, Time-resolved photoluminescence spectroscopy, THz spectroscopy setup, Electro-optic sampling, Optical pump - THz probe spectroscopy, THz time-domain spectroscopy).

Author Information

Corresponding author

Agustin Schiffrin — *School of Physics and Astronomy, Monash University, Clayton, 3800, VIC, Australia*; orcid.org/0000-0003-1140-8485; Email: agustin.schiffrin@monash.edu

Authors

Mitko Oldfield — *School of Physics and Astronomy, Monash University, Clayton, 3800, VIC, Australia*; orcid.org/0000-0002-8928-6556; Email: mitko.oldfield@monash.edu

Gary Beane — *School of Physics and Astronomy, Monash University, Clayton, 3800, VIC, Australia*; orcid.org/0000-0001-5312-0477; Email: gary.beane@monash.edu

Sebastian Fürer — *School of Engineering, Monash University, Clayton, 3800, VIC, Australia*; orcid.org/0000-0003-3954-4657

Tan-Phat Nguyen — *School of Physics and Astronomy, Monash University, Clayton, 3800, VIC, Australia*; orcid.org/0000-0002-6929-9376

Philippe Holzhey — *Department of Physics, University of Oxford, Oxford, OX1 3PJ, United Kingdom*; orcid.org/0000-0003-3688-1607; Email: philippe.holzhey@physics.ox.ac.uk

Boer Tan — *Oxford PV, Kidlington, OX5 1QU, United Kingdom*; orcid.org/0000-0003-1123-7786

Wenxin Mao — *Department of Chemical Engineering and Biotechnology, University of Cambridge, Cambridge, CB3 OAS, United Kingdom*; orcid.org/0000-0002-3675-829X

Henry Snaith — *Department of Physics, University of Oxford, Oxford, OX1 3PJ, United Kingdom*; orcid.org/0000-0001-8511-790X

Udo Bach — *School of Engineering, Monash University, Clayton, 3800, VIC, Australia*; orcid.org/0000-0003-2922-4959; Email: udo.bach@monash.edu

Notes The authors declare no competing interests.

Acknowledgement

This work was supported by the ARC Centre of Excellence in Future Low-Energy Electronics Technologies (FLEET, CE170100039) as well as the ARC Centre of Excellence in Exciton Science (CE170100026). This research was conducted at Monash University and was made possible via the Monash Faculty of Science Dean's International Postgraduate Research Scholarship (MIPRS) and the FLEET PhD Top-Up Scholarship. We thank the Melbourne

Centre for Nanofabrication, the Monash X-ray Platform and the Monash Centre for Electron Microscopy for the use of their facilities.

References

(1) Fakharuddin, A.; Gangishetty, M. K.; Abdi-Jalebi, M.; Chin, S.-H.; bin Mohd Yusoff, A. R.; Congreve, D. N.; Tress, W.; Deschler, F.; Vasilopoulou, M.; Bolink, H. J. Perovskite light-emitting diodes. *Nature Electronics* **2022**, *5*, 203–216.

(2) (NREL), N. R. E. L. Best Research-Cell Efficiencies. online, 2023; `https://www.nrel.gov/pv/cell-efficiency.html`.

(3) Saliba, M.; Matsui, T.; Seo, J.-Y.; Domanski, K.; Correa-Baena, J.-P.; Nazeeruddin, M. K.; Zakeeruddin, S. M.; Tress, W.; Abate, A.; Hagfeldt, A.; Grätzel, M. Cesium-containing triple cation perovskite solar cells: improved stability, reproducibility and high efficiency. *Energy Environ. Sci.* **2016**, *9*, 1989–1997.

(4) Masi, S.; Gualdrón-Reyes, A. F.; Mora-Seró, I. Stabilization of Black Perovskite Phase in $FAPbI_3$ and $CsPbI_3$. *ACS Energy Lett.* **2020**, *5*, 1974–1985.

(5) Protesescu, L.; Yakunin, S.; Kumar, S.; Bär, J.; Bertolotti, F.; Masciocchi, N.; Guagliardi, A.; Grotevent, M.; Shorubalko, I.; Bodnarchuk, M. I.; Shih, C.-J.; Kovalenko, M. V. Dismantling the "Red Wall" of Colloidal Perovskites: Highly Luminescent Formamidinium and Formamidinium-Cesium Lead Iodide Nanocrystals. *ACS Nano* **2017**, *11*, 3119–3134.

(6) Akbulatov, A. F.; Ustinova, M. I.; Gutsev, L.; Tsarev, S. A.; Dremova, N. N.; Zhidkov, I.; Luchkin, S. Y.; Ramachandran, B. R.; Frolova, L.; Kurmaev, E. Z.; Stevenson, K. J.; Aldoshin, S. M.; Troshin, P. A. When iodide meets bromide: Halide mixing facilitates the light-induced decomposition of perovskite absorber films. *Nano Energy* **2021**, *86*, 106082.

(7) Zhang, Y.; Chen, M.; Zhou, Y.; Li, W.; Lee, Y.; Kanda, H.; Gao, X.-X.; Hu, R.; Brooks, K. G.; Zia, R.; Kinge, S.; Padture, N. P.; Nazeeruddin, M. K. The Synergism of DMSO and Diethyl Ether for Highly Reproducible and Efficient $MA_{0.5}FA_{0.5}PbI_3$ Perovskite Solar Cells. *Advanced Energy Materials* **2020**, *10*, 2001300.

(8) Zhang, T. et al. Ion-modulated radical doping of spiro-OMeTAD for more efficient and stable perovskite solar cells. *Science* **2022**, *377*, 495–501.

(9) Zhang, F. et al. Metastable Dion-Jacobson 2D structure enables efficient and stable perovskite solar cells. *Science* **2022**, *375*, 71–76.

(10) Zheng, X.; Wu, C.; Jha, S. K.; Li, Z.; Zhu, K.; Priya, S. Improved Phase Stability of Formamidinium Lead Triiodide Perovskite by Strain Relaxation. *ACS Energy Lett.* **2016**, *1*, 1014–1020.

(11) Kim, M.; Kim, G.-H.; Lee, T. K.; Choi, I. W.; Choi, H. W.; Jo, Y.; Yoon, Y. J.; Kim, J. W.; Lee, J.; Huh, D.; Lee, H.; Kwak, S. K.; Kim, J. Y.; Kim, D. S. Methylammonium Chloride Induces Intermediate Phase Stabilization for Efficient Perovskite Solar Cells. *Joule* **2019**, *3*, 2179–2192.

(12) Alsalloum, A. Y.; Turedi, B.; Zheng, X.; Mitra, S.; Zhumekenov, A. A.; Lee, K. J.; Maity, P.; Gereige, I.; AlSaggaf, A.; Roqan, I. S.; Mohammed, O. F.; Bakr, O. M. Low-Temperature Crystallization Enables 21.9% Efficient Single-Crystal $MAPbI_3$ Inverted Perovskite Solar Cells. *ACS Energy Letters* **2020**, *5*, 657–662.

(13) Chen, Z.; Turedi, B.; Alsalloum, A. Y.; Yang, C.; Zheng, X.; Gereige, I.; AlSaggaf, A.; Mohammed, O. F.; Bakr, O. M. Single-Crystal $MAPbI_3$ Perovskite Solar Cells Exceeding 21% Power Conversion Efficiency. *ACS Energy Letters* **2019**, *4*, 1258–1259.

(14) Lu, R.; Liu, Y.; Zhang, J.; Zhao, D.; Guo, X.; Li, C. Highly efficient (200) oriented $MAPbI_3$ perovskite solar cells. *Chemical Engineering Journal* **2022**, *433*, 133845.

(15) Huang, Y.; Lei, X.; He, T.; Jiang, Y.; Yuan, M. Recent Progress on Formamidinium-Dominated Perovskite Photovoltaics. *Advanced Energy Materials* **2022**, *12*, 2100690.

(16) Jeong, M.; Choi, I. W.; Go, E. M.; Cho, Y.; Kim, M.; Lee, B.; Jeong, S.; Jo, Y.; Choi, H. W.; Lee, J.; Bae, J.-H.; Kwak, S. K.; Kim, D. S.; Yang, C. Stable perovskite solar cells with efficiency exceeding 24.8% and 0.3-V voltage loss. *Science* **2020**, *369*, 1615–1620.

(17) Kim, M. et al. Conformal quantum dot–SnO_2 layers as electron transporters for efficient perovskite solar cells. *Science* **2022**, *375*, 302–306.

(18) Yoo, J. J.; Seo, G.; Chua, M. R.; Park, T. G.; Lu, Y.; Rotermund, F.; Kim, Y.-K.; Moon, C. S.; Jeon, N. J.; Correa-Baena, J.-P.; Bulović, V.; Shin, S. S.; Bawendi, M. G.; Seo, J. Efficient perovskite solar cells via improved carrier management. *Nature* **2021**, *590*, 587–593.

(19) Zhang, T. et al. Ion-modulated radical doping of spiro-OMeTAD for more efficient and stable perovskite solar cells. *Science* **2022**, *377*, 495–501.

(20) Jeong, M.; Choi, I. W.; Yim, K.; Jeong, S.; Kim, M.; Choi, S. J.; Cho, Y.; An, J.-H.; Kim, H.-B.; Jo, Y.; Kang, S.-H.; Bae, J.-H.; Lee, C.-W.; Kim, D. S.; Yang, C. Large-area perovskite solar cells employing spiro-Naph hole transport material. *Nature Photonics* **2022**, *16*, 119–125.

(21) Wang, Y.; Liang, Y.; Zhang, Y.; Yang, W.; Sun, L.; Xu, D. Pushing the Envelope: Achieving an Open-Circuit Voltage of 1.18 V for Unalloyed $MAPbI_3$ Perovskite Solar Cells of a Planar Architecture. *Advanced Functional Materials* **2018**, *28*, 1801237.

(22) Kim, M.; woo Choi, I.; Choi, S. J.; Song, J. W.; Mo, S.-I.; An, J.-H.; Jo, Y.; Ahn, S.; Ahn, S. K.; Kim, G.-H.; Kim, D. S. Enhanced electrical properties of Li-salts doped mesoporous TiO_2 in perovskite solar cells. *Joule* **2021**, *5*, 659–672.

(23) Li, J.; Dagar, J.; Shargaieva, O.; Flatken, M. A.; Köbler, H.; Fenske, M.; Schultz, C.; Stegemann, B.; Just, J.; Többens, D. M.; Abate, A.; Munir, R.; Unger, E. 20.8% Slot-Die Coated $MAPbI_3$ Perovskite Solar Cells by Optimal DMSO-Content and Age of 2-ME Based Precursor Inks. *Advanced Energy Materials* **2021**, *11*, 2003460.

(24) Li, N.; Feng, A.; Guo, X.; Wu, J.; Xie, S.; Lin, Q.; Jiang, X.; Liu, Y.; Chen, Z.; Tao, X. Engineering the Hole Extraction Interface Enables Single-Crystal MAPbI3 Perovskite Solar Cells with Efficiency Exceeding 22% and Superior Indoor Response. *Advanced Energy Materials* **2022**, *12*, 2103241.

(25) Liu, Z.; Krückemeier, L.; Krogmeier, B.; Klingebiel, B.; Márquez, J. A.; Levcenko, S.; Öz, S.; Mathur, S.; Rau, U.; Unold, T.; Kirchartz, T. Open-Circuit Voltages Exceeding 1.26 V in Planar Methylammonium Lead Iodide Perovskite Solar Cells. *ACS Energy Letters* **2019**, *4*, 110–117.

(26) Shin, S. S.; Yeom, E. J.; Yang, W. S.; Hur, S.; Kim, M. G.; Im, J.; Seo, J.; Noh, J. H.; Seok, S. I. Colloidally prepared La-doped $BaSnO_3$ electrodes for efficient, photostable perovskite solar cells. *Science* **2017**, *356*, 167–171.

(27) Jeong, J. et al. Pseudo-halide anion engineering for α-$FAPbI_3$ perovskite solar cells. *Nature* **2021**, *592*, 381–385.

(28) Yun, H.-S.; Kwon, H. W.; Paik, M. J.; Hong, S.; Kim, J.; Noh, E.; Park, J.; Lee, Y.; Il Seok, S. Ethanol-based green-solution processing of α-formamidinium lead triiodide perovskite layers. *Nature Energy* **2022**, *7*, 828–834.

(29) Min, H.; Ji, S.-G.; Seok, S. I. Relaxation of externally strained halide perovskite thin layers with neutral ligands. *Joule* **2022**, *6*, 2175–2185.

(30) Min, H.; Lee, D. Y.; Kim, J.; Kim, G.; Lee, K. S.; Kim, J.; Paik, M. J.; Kim, Y. K.; Kim, K. S.; Kim, M. G.; Shin, T. J.; Il Seok, S. Perovskite solar cells with atomically coherent interlayers on SnO_2 electrodes. *Nature* **2021**, *598*, 444–450.

(31) Parida, B.; Yoon, S.; Ryu, J.; Hayase, S.; Jeong, S. M.; Kang, D.-W. Boosting the Conversion Efficiency Over 20.

(32) Min, H.; Kim, M.; Lee, S.-U.; Kim, H.; Kim, G.; Choi, K.; Lee, J. H.; Seok, S. I. Efficient, stable solar cells by using inherent bandgap of α-phase formamidinium lead iodide. *Science* **2019**, *366*, 749–753.

(33) Kim, G.; Min, H.; Lee, K. S.; Lee, D. Y.; Yoon, S. M.; Seok, S. I. Impact of strain relaxation on performance of α-formamidinium lead iodide perovskite solar cells. *Science* **2020**, *370*, 108–112.

(34) Ma, C.; Kang, M.-C.; Lee, S.-H.; Kwon, S. J.; Cha, H.-W.; Yang, C.-W.; Park, N.-G. Photovoltaically top-performing perovskite crystal facets. *Joule* **2022**, *6*, 2626–2643.

(35) Tan, S. et al. Stability-limiting heterointerfaces of perovskite photovoltaics. *Nature* **2022**, *605*, 268–273.

(36) Zhao, L. et al. Chemical Polishing of Perovskite Surface Enhances Photovoltaic Performances. *J. Am. Chem. Soc.* **2022**, *144*, 1700–1708.

(37) Jiang, Q. et al. Surface reaction for efficient and stable inverted perovskite solar cells. *Nature* **2022**, *611*, 278–283.

(38) Zhang, F. et al. Metastable Dion-Jacobson 2D structure enables efficient and stable perovskite solar cells. *Science* **2022**, *375*, 71–76.

(39) Stranks, S. D.; Burlakov, V. M.; Leijtens, T.; Ball, J. M.; Goriely, A.; Snaith, H. J. Recombination Kinetics in Organic-Inorganic Perovskites: Excitons, Free Charge, and Subgap States. *Phys. Rev. Appl.* **2014**, *2*, 034007.

(40) Zhao, D.; Chia, E. E. M. Free Carrier, Exciton, and Phonon Dynamics in Lead-Halide Perovskites Studied with Ultrafast Terahertz Spectroscopy. *Advanced Optical Materials* **2020**, *8*, 1900783.

(41) Zhang, H.; Debroye, E.; Vina-Bausa, B.; Valli, D.; Fu, S.; Zheng, W.; Di Virgilio, L.; Gao, L.; Frost, J. M.; Walsh, A.; Hofkens, J.; Wang, H. I.; Bonn, M. Stable Mott Polaron State Limits the Charge Density in Lead Halide Perovskites. *ACS Energy Lett.* **2023**, *8*, 420–428.

(42) Sun, Q.; Liu, X.; Cao, J.; Stantchev, R. I.; Zhou, Y.; Chen, X.; Parrott, E. P. J.; Lloyd-Hughes, J.; Zhao, N.; Pickwell-MacPherson, E. Highly Sensitive Terahertz Thin-Film Total Internal Reflection Spectroscopy Reveals in Situ Photoinduced Structural Changes in Methylammonium Lead Halide Perovskites. *J. Phys. Chem. C* **2018**, *122*, 17552–17558.

(43) Hempel, H. et al. Predicting Solar Cell Performance from Terahertz and Microwave Spectroscopy. *Adv. Energy Mater.* **2022**, *12*, 2102776.

(44) Rehman, Waqaas and Milot, R. and Eperon, G. and Wehrenfennig, C. and Boland, J. L. and Snaith, H. and Johnston, M. and Herz, L. Charge-Carrier Dynamics and Mobilities in Formamidinium Lead Mixed-Halide Perovskites. *Advanced Materials* **2015**, *27 48*, 7938–44.

(45) Rehman, W.; McMeekin, D. P.; Patel, J. B.; Milot, R. L.; Johnston, M. B.; Snaith, H. J.; Herz, L. M. Photovoltaic mixed-cation lead mixed-halide perovskites: links between crystallinity, photo-stability and electronic properties. *Energy Environ. Sci.* **2017**, *10*, 361–369.

(46) Yin, W.-J.; Shi, T.; Yan, Y. Unusual defect physics in CH3NH3PbI3 perovskite solar cell absorber. *Applied Physics Letters* **2014**, *104*, 063903.

(47) Deschler, F.; Price, M.; Pathak, S.; Klintberg, L. E.; Jarausch, D.-D.; Higler, R.; Hüttner, S.; Leijtens, T.; Stranks, S. D.; Snaith, H. J.; Atatüre, M.; Phillips, R. T.; Friend, R. H. High Photoluminescence Efficiency and Optically Pumped Lasing in

Solution-Processed Mixed Halide Perovskite Semiconductors. *J. Phys. Chem. Lett.* **2014**, *5*, 1421–1426.

(48) Herz, L. M. Charge-Carrier Dynamics in Organic-Inorganic Metal Halide Perovskites. *Annual Review of Physical Chemistry* **2016**, *67*, 65–89.

(49) Luo, D.; Su, R.; Zhang, W.; Gong, Q.; Zhu, R. Minimizing non-radiative recombination losses in perovskite solar cells. *Nature Reviews Materials* **2020**, *5*, 44–60.

(50) Chantana, J.; Kawano, Y.; Nishimura, T.; Mavlonov, A.; Shen, Q.; Yoshino, K.; Iikubo, S.; Hayase, S.; Minemoto, T. Impact of Auger recombination on performance limitation of perovskite solar cell. *Solar Energy* **2021**, *217*, 342–353.

(51) Zhao, F.; Ren, A.; Li, P.; Li, Y.; Wu, J.; Wang, Z. M. Toward Continuous-Wave Pumped Metal Halide Perovskite Lasers: Strategies and Challenges. *ACS Nano* **2022**, *16*, 7116–7143.

(52) Allegro, I.; Li, Y.; Richards, B. S.; Paetzold, U. W.; Lemmer, U.; Howard, I. A. Bimolecular and Auger Recombination in Phase-Stable Perovskite Thin Films from Cryogenic to Room Temperature and Their Effect on the Amplified Spontaneous Emission Threshold. *The Journal of Physical Chemistry Letters* **2021**, *12*, 2293–2298, PMID: 33651626.

(53) Reid, O. G.; Yang, M.; Kopidakis, N.; Zhu, K.; Rumbles, G. Grain-Size-Limited Mobility in Methylammonium Lead Iodide Perovskite Thin Films. *ACS Energy Lett.* **2016**, *1*, 561–565.

(54) Guse, J. A.; Soufiani, A. M.; Jiang, L.; Kim, J.; Cheng, Y.-B.; Schmidt, T. W.; Ho-Baillie, A.; McCamey, D. R. Spectral dependence of direct and trap-mediated recombination processes in lead halide perovskites using time resolved microwave conductivity. *Phys. Chem. Chem. Phys.* **2016**, *18*, 12043–12049.

(55) Nie, W.; Tsai, H.; Asadpour, R.; Blancon, J.-C.; Neukirch, A. J.; Gupta, G.; Crochet, J. J.; Chhowalla, M.; Tretiak, S.; Alam, M. A.; Wang, H.-L.; Mohite, A. D. High-efficiency solution-processed perovskite solar cells with millimeter-scale grains. *Science* **2015**, *347*, 522–525.

(56) Zhumekenov, A. A.; Saidaminov, M. I.; Haque, M. A.; Alarousu, E.; Sarmah, S. P.; Murali, B.; Dursun, I.; Miao, X.-H.; Abdelhady, A. L.; Wu, T.; Mohammed, O. F.; Bakr, O. M. Formamidinium Lead Halide Perovskite Crystals with Unprecedented Long Carrier Dynamics and Diffusion Length. *ACS Energy Lett.* **2016**, *1*, 32–37.

(57) Han, Q.; Bae, S.-H.; Sun, P.; Hsieh, Y.-T.; Yang, Y. M.; Rim, Y. S.; Zhao, H.; Chen, Q.; Shi, W.; Li, G.; Yang, Y. Single Crystal Formamidinium Lead Iodide ($FAPbI_3$): Insight into the Structural, Optical, and Electrical Properties. *Advanced Materials* **2016**, *28*, 2253–2258.

(58) Lim, J.; Kober-Czerny, M.; Lin, Y.-H.; Ball, J. M.; Sakai, N.; Duijnstee, E. A.; Hong, M. J.; Labram, J. G.; Wenger, B.; Snaith, H. J. Long-range charge carrier mobility in metal halide perovskite thin-films and single crystals via transient photoconductivity. *Nature Communications* **2022**, *13*, 4201.

(59) Crothers, T. W.; Milot, R. L.; Patel, J. B.; Parrott, E. S.; Schlipf, J.; Müller-Buschbaum, P.; Johnston, M. B.; Herz, L. M. Photon Reabsorption Masks Intrinsic Bimolecular Charge-Carrier Recombination in CH3NH3PbI3 Perovskite. *Nano Lett.* **2017**, *17*, 5782–5789.

(60) Kober-Czerny, M.; Motti, S. G.; Holzhey, P.; Wenger, B.; Lim, J.; Herz, L. M.; Snaith, H. J. Excellent Long-Range Charge-Carrier Mobility in 2D Perovskites. *Advanced Functional Materials* **2022**, *32*, 2203064.

(61) Eperon, G. E.; Stranks, S. D.; Menelaou, C.; Johnston, M. B.; Herz, L. M.;

Snaith, H. J. Formamidinium lead trihalide: a broadly tunable perovskite for efficient planar heterojunction solar cells. *Energy Environ. Sci.* **2014**, *7*, 982–988.

(62) Marongiu, D.; Saba, M.; Quochi, F.; Mura, A.; Bongiovanni, G. The role of excitons in 3D and 2D lead halide perovskites. *J. Mater. Chem. C* **2019**, *7*, 12006–12018.

(63) Sestu, N.; Cadelano, M.; Sarritzu, V.; Chen, F.; Marongiu, D.; Piras, R.; Mainas, M.; Quochi, F.; Saba, M.; Mura, A.; Bongiovanni, G. Absorption F-Sum Rule for the Exciton Binding Energy in Methylammonium Lead Halide Perovskites. *J. Phys. Chem. Lett.* **2015**, *6*, 4566–4572.

(64) Fang, H.-H.; Wang, F.; Adjokatse, S.; Zhao, N.; Even, J.; Loi, M. A. Photoexcitation dynamics in solution-processed formamidinium lead iodide perovskite thin films for solar cell applications. *Light: Science & Applications* **2016**, *5*, e16056–e16056.

(65) Niedzwiedzki, D. M.; Zhou, H.; Biswas, P. Exciton Binding Energy of MAPbI3 Thin Film Elucidated via Analysis and Modeling of Perovskite Absorption and Photoluminescence Properties Using Various Methodologies. *Journal of Physical Chemistry C* **2022**, *126*, 1046–1054.

(66) Yang, J. et al. Acoustic-optical phonon up-conversion and hot-phonon bottleneck in lead-halide perovskites. *Nature Communications* **2017**, *8*, 14120.

(67) Yang, Y.; Yang, M.; Li, Z.; Crisp, R.; Zhu, K.; Beard, M. C. Comparison of Recombination Dynamics in $CH_3NH_3PbBr_3$ and $CH_3NH_3PbI_3$ Perovskite Films: Influence of Exciton Binding Energy. *J. Phys. Chem. Lett.* **2015**, *6*, 4688–4692.

(68) D'Innocenzo, V.; Grancini, G.; Alcocer, M. J. P.; Kandada, A. R. S.; Stranks, S. D.; Lee, M. M.; Lanzani, G.; Snaith, H. J.; Petrozza, A. Excitons versus free charges in organo-lead tri-halide perovskites. *Nature Communications* **2014**, *5*, 3586.

(69) Wu, K.; Bera, A.; Ma, C.; Du, Y.; Yang, Y.; Li, L.; Wu, T. Temperature-dependent excitonic photoluminescence of hybrid organometal halide perovskite films. *Physical Chemistry Chemical Physics* **2014**, *16*, 22476–22481.

(70) Muhammad, Z.; Rashid, A. Exciton binding energies and polaron interplay in the optically excited state of organic-inorganic lead halide perovskites. *Materials Advances* **2024**, 13–38.

(71) Sum, T. C.; Mathews, N.; Xing, G.; Lim, S. S.; Chong, W. K.; Giovanni, D.; Dewi, H. A. Spectral Features and Charge Dynamics of Lead Halide Perovskites: Origins and Interpretations. *Accounts of Chemical Research* **2016**, *49*, 294–302, PMID: 26820796.

(72) Péan, E. V.; Dimitrov, S.; De Castro, C. S.; Davies, M. L. Interpreting time-resolved photoluminescence of perovskite materials. *Phys. Chem. Chem. Phys.* **2020**, *22*, 28345–28358.

(73) Wehrenfennig, C.; Liu, M.; Snaith, H. J.; Johnston, M. B.; Herz, L. M. Charge-carrier dynamics in vapour-deposited films of the organolead halide perovskite $CH_3NH_3PbI_{3-x}Cl_x$. *Energy Environ. Sci.* **2014**, *7*, 2269–2275.

(74) Eperon, G. E.; Jedlicka, E.; Ginger, D. S. Biexciton Auger Recombination Differs in Hybrid and Inorganic Halide Perovskite Quantum Dots. *J. Phys. Chem. Lett.* **2018**, *9*, 104–109.

(75) Fu, J.; Xu, Q.; Han, G.; Wu, B.; Huan, C. H. A.; Leek, M. L.; Sum, T. C. Hot carrier cooling mechanisms in halide perovskites. *Nature Communications* **2017**, *8*, 1300.

(76) Staub, F.; Hempel, H.; Hebig, J.-C.; Mock, J.; Paetzold, U. W.; Rau, U.; Unold, T.; Kirchartz, T. Beyond Bulk Lifetimes: Insights into Lead Halide Perovskite Films from Time-Resolved Photoluminescence. *Phys. Rev. Appl.* **2016**, *6*, 044017.

(77) Feldmann, S. et al. Photodoping through local charge carrier accumulation in alloyed hybrid perovskites for highly efficient luminescence. *Nature Photonics* **2020**, *14*, 123–128.

(78) Richter, J. M.; Abdi-Jalebi, M.; Sadhanala, A.; Tabachnyk, M.; Rivett, J. P. H.; Pazos-Outón, L. M.; Gödel, K. C.; Price, M.; Deschler, F.; Friend, R. H. Enhancing photoluminescence yields in lead halide perovskites by photon recycling and light outcoupling. *Nature Communications* **2016**, *7*, 13941.

(79) Herz, L. M. Charge-Carrier Mobilities in Metal Halide Perovskites: Fundamental Mechanisms and Limits. *ACS Energy Lett.* **2017**, *2*, 1539–1548.

(80) Khmelevskaia, D.; Markina, D.; Tonkaev, P.; Masharin, M.; Peltek, A.; Talianov, P.; Baranov, M. A.; Nikolaeva, A.; Zyuzin, M. V.; Zelenkov, L. E.; Pushkarev, A. P.; Rogach, A. L.; Makarov, S. V. Excitonic versus Free-Carrier Contributions to the Nonlinearly Excited Photoluminescence in $CsPbBr_3$ Perovskites. *ACS Photonics* **2022**, *9*, 179–189.

(81) Kim, J. Y.; Lee, J.-W.; Jung, H. S.; Shin, H.; Park, N.-G. High-Efficiency Perovskite Solar Cells. *Chem. Rev.* **2020**, *120*, 7867–7918.

(82) Ščajev, P.; Miasojedovas, S.; Juršėnas, S. A carrier density dependent diffusion coefficient, recombination rate and diffusion length in MAPbI3 and MAPbBr3 crystals measured under one- and two-photon excitations. *J. Mater. Chem. C* **2020**, *8*, 10290–10301.

(83) Long, R.; Liu, J.; Prezhdo, O. V. Unravelling the Effects of Grain Boundary and Chemical Doping on Electron-Hole Recombination in CH3NH3PbI3 Perovskite by Time-Domain Atomistic Simulation. *J. Am. Chem. Soc.* **2016**, *138*, 3884–3890.

(84) Kim, H. D.; Ohkita, H.; Benten, H.; Ito, S. Photovoltaic Performance of Perovskite Solar Cells with Different Grain Sizes. *Advanced Materials* **2016**, *28*, 917–922.

(85) Xia, C. Q.; Peng, J.; Poncé, S.; Patel, J. B.; Wright, A. D.; Crothers, T. W.; Uller Rothmann, M.; Borchert, J.; Milot, R. L.; Kraus, H.; Lin, Q.; Giustino, F.; Herz, L. M.; Johnston, M. B. Limits to Electrical Mobility in Lead-Halide Perovskite Semiconductors. *The Journal of Physical Chemistry Letters* **2021**, *12*, 3607–3617, PMID: 33822630.

(86) Zhu, H.; Miyata, K.; Fu, Y.; Wang, J.; Joshi, P. P.; Niesner, D.; Williams, K. W.; Jin, S.; Zhu, X.-Y. Screening in crystalline liquids protects energetic carriers in hybrid perovskites. *Science* **2016**, *353*, 1409–1413.

(87) Chen, T.; Chen, W.-L.; Foley, B. J.; Lee, J.; Ruff, J. P. C.; Ko, J. Y. P.; Brown, C. M.; Harriger, L. W.; Zhang, D.; Park, C.; Yoon, M.; Chang, Y.-M.; Choi, J. J.; Lee, S.-H. Origin of long lifetime of band-edge charge carriers in organic-inorganic lead iodide perovskites. *Proceedings of the National Academy of Sciences of the United States of America* **2017**, *114*, 7519–7524.

(88) Dubajic, M. et al. Dynamic nanodomains dictate macroscopic properties in lead halide perovskites. *Nature Nanotechnology* **2025**, *20*, 755–763.

(89) La-o vorakiat, C.; Xia, H.; Kadro, J.; Salim, T.; Zhao, D.; Ahmed, T.; Lam, Y. M.; Zhu, J.-X.; Marcus, R. A.; Michel-Beyerle, M.-E.; Chia, E. E. M. Phonon Mode Transformation Across the Orthohombic–Tetragonal Phase Transition in a Lead Iodide Perovskite $CH_3NH_3PbI_3$: A Terahertz Time-Domain Spectroscopy Approach. *The Journal of Physical Chemistry Letters* **2016**, *7*, 1–6, PMID: 26633131.

(90) Leguy, A. M. A.; Goñi, A. R.; Frost, J. M.; Skelton, J.; Brivio, F.; Rodríguez-Martínez, X.; Weber, O. J.; Pallipurath, A.; Alonso, M. I.; Campoy-Quiles, M.; Weller, M. T.; Nelson, J.; Walsh, A.; Barnes, P. R. F. Dynamic disorder, phonon lifetimes, and the assignment of modes to the vibrational spectra of methylammonium lead halide perovskites. *Phys. Chem. Chem. Phys.* **2016**, *18*, 27051–27066.

(91) Carignano, M. A.; Saeed, Y.; Aravindh, S. A.; Roqan, I. S.; Even, J.; Katan, C. A close examination of the structure and dynamics of $HC(NH_2)_2PbI_3$ by MD simulations and group theory. *Phys. Chem. Chem. Phys.* **2016**, *18*, 27109–27118.

(92) Feynman, R. P.; Hellwarth, R. W.; Iddings, C. K.; Platzman, P. M. Mobility of Slow Electrons in a Polar Crystal. *Phys. Rev.* **1962**, *127*, 1004–1017.

(93) Hellwarth, R. W.; Biaggio, I. Mobility of an electron in a multimode polar lattice. *Phys. Rev. B* **1999**, *60*, 299–307.

(94) Menéndez-Proupin, E.; Beltrán Ríos, C. L.; Wahnón, P. Nonhydrogenic exciton spectrum in perovskite CH3NH3PbI3. *physica status solidi (RRL) – Rapid Research Letters* **2015**, *9*, 559–563.

(95) Devreese, J. T.; Alexandrov, A. S. Fröhlich polaron and bipolaron: recent developments. *Reports on Progress in Physics* **2009**, *72*, 066501.

(96) Cochran, W.; Cowley, R. Dielectric constants and lattice vibrations. *Journal of Physics and Chemistry of Solids* **1962**, *23*, 447–450.

(97) Sendner, M.; Nayak, P. K.; Egger, D. A.; Beck, S.; Müller, C.; Epding, B.; Kowalsky, W.; Kronik, L.; Snaith, H. J.; Pucci, A.; Lovrinčić, R. Optical phonons in methylammonium lead halide perovskites and implications for charge transport. *Mater. Horiz.* **2016**, *3*, 613–620.

(98) Zhao, D.; Skelton, J. M.; Hu, H.; La-o vorakiat, C.; Zhu, J.-X.; Marcus, R. A.; Michel-Beyerle, M.-E.; Lam, Y. M.; Walsh, A.; Chia, E. E. M. Low-frequency optical phonon modes and carrier mobility in the halide perovskite $CH_3NH_3PbBr_3$ using terahertz time-domain spectroscopy. *Applied Physics Letters* **2017**, *111*, 201903.

(99) Li, H. et al. Enhanced Hot-Phonon Bottleneck Effect on Slowing Hot Carrier Cooling

in Metal Halide Perovskite Quantum Dots with Alloyed A-Site. *Advanced Materials* **2023**, *35*, 2301834.

(100) Fu, M.; Tamarat, P.; Trebbia, J.-B.; Bodnarchuk, M. I.; Kovalenko, M. V.; Even, J.; Lounis, B. Unraveling exciton-phonon coupling in individual $FAPbI_3$ nanocrystals emitting near-infrared single photons. *Nature Communications* **2018**, *9*, 3318.

(101) Valverde-Chávez, D. A.; Ponseca, C. S.; Stoumpos, C. C.; Yartsev, A.; Kanatzidis, M. G.; Sundström, V.; Cooke, D. G. Intrinsic femtosecond charge generation dynamics in single crystal CH3NH3PbI3. *Energy Environ. Sci.* **2015**, *8*, 3700–3707.

TOC Graphic